Fermilab Library
0 1160 0052511 7

SDC-90-00097

SDC
SOLENOIDAL DETECTOR NOTES

MOMENTUM RESOLUTION IN A NONUNIFORM MAGNETIC FIELD

Hiroyuki Iwasaki

Presented at 1990 Summer Study on High Energy Physics,
Snowmass, June 25-July 13, 1990;
Revised for JSD Workshop, KEK, Aug 8-9, 1990.

SDC-90-00097

JSD - NOTE - 1990 - 48

Momentum resolution in a nonuniform magnetic field

Hiroyuki Iwasaki

KEK, Tsukuba, Ibaraki, JAPAN

Representing a study group on nonuniform magnetic fields [1]

Abstract

We studied the momentum resolution in a nonuniform solenoidal magnetic field. In the calculation, we assumed the tracking devices and their position resolutions were those given in the Expression of Interest (EOI) of the Solenoidal Detector Collaboration (SDC) [2]. The momentum resolution for high-p_t tracks in a field of Type-S is the same as that of in the uniform field up to $|\eta| = 1$ (η is the pseudorapidity, $\eta = -\ln\tan(\theta/2)$), and 20 to 30% worse in $1.6 < |\eta| < 2.5$. We also studied a coil with graded current density, effectiveness of the vertex constraint fit, and dependence on the tracking volume.

Presented at 1990 Summer Study on High Energy Physics, Snowmass, Colorado, June 25 - July 13, 1990; Revised for JSD Workshop, KEK, August 8 - 9, 1990.

1 Introduction

In designing a general purpose 4π detector, it is sometimes controversial whether it should be with a magnetic field or without. Even with a magnetic field, there are many branches, such as (a) dipole or solenoid, (b) outside or inside of the calorimeter, (c) uniform or nonuniform. Here, we assume the case of a solenoidal magnet with the coil being inside the calorimeter. There are still some choices for the field uniformity. The uniform field is preferable for the tracking purpose. However, it heavily imposes constraints on a design of the calorimeter system.

Merits of the uniform field could be (i) easiness of pattern recognition, (ii) better momentum resolution, (iii) saving CPU time because of a simple circle trajectory for any track, (iv) sharp p_t-cut in a track trigger. Indeed these points are qualitatively true, but not based on quantitative arguments so far. In this report, we will study the p_t resolution in a nonuniform field for high-p_t tracks. In particular, we will concentrate on the Type-S option in EOI of the SDC group.

2 Methodology

2.1 Trajectory of a high-p_t track

Equation of motion of a charged particle in a magnetic field, $\vec{B}$, is

$$\frac{d\vec{p}}{dt} = q\vec{v} \times \vec{B}, \tag{1}$$

where q is the charge of the particle. The trajectory of a high-p_t track is almost straight. For example, a charged track of 1 TeV/c in a uniform field of 2 tesla will deviate only 1.2 mm from a straight line after a flight of 2 m. In this limit, one can easily get the analytical solution of equation (1).

We define the standard coordinate system such that the origin is the center of the solenoidal coil, the z-axis is parallel to the coil, and $+z$ is the direction of the magnetic field. We assume that a track is ejected from near the origin and close to the x-axis. The boundary conditions are

$$\left.\begin{array}{l} y = \delta \\ dy/dx = \phi \end{array}\right\} \text{ at } x = 0, \tag{2}$$

with $\delta \ll$ coil radius, and $\phi \ll 1$. The solution is then,

$$y = \delta + \phi x - \frac{q}{p_t}\int_0^x dx' \int_0^{x'} dx''\, B(x''; \theta), \tag{3}$$

$$B(x;\theta) = B_z - B_x \cot\theta, \tag{4}$$

where θ is the polar angle of the track, $z = x\cot\theta$. If we define c as

$$c \equiv \frac{qB_0}{p_t}, \tag{5}$$

where B_0 is the field strength at the origin, $B_0 = B(0;\theta)$, then c represents the curvature of the track at the origin. Because

$$\frac{d^2y}{dx^2} = -\frac{qB_0}{p_t} = -c.$$

Finally, we define

$$I(x;\theta) \equiv \frac{2}{B_0}\int_0^x dx' \int_0^{x'} dx''\, B(x''; \theta), \tag{6}$$

then, we get a transparent formula for a trajectory

$$y = \delta + \phi x - \frac{1}{2} c\, I(x;\theta). \tag{7}$$

For the uniform field, for example, the integration is easily calculated and we get

$$y = \delta + \phi x - \frac{1}{2} c\, x^2,$$

which is the familiar expression of a circle trajectory.

2.2 Fitting procedure

As for the evaluation of the momentum resolution, we followed the method of R. L. Gluckstern [3], and extended the formula for a nonuniform magnetic field. We assume that a trajectory is measured at $x = x_n$ $(n = 1, 2, ..., N)$ as $y = y_n$ with *rms* error σ_n. We want to fit these points with equation (7), and determine the coefficients δ, ϕ, and c. The chi-square is defined as

$$\chi^2 \equiv \sum_{i=1}^{N} [\frac{1}{\sigma_n^2}(y_n - \delta - \phi x_n + \frac{1}{2} c I_n)^2], \tag{8}$$

where $I_n \equiv I(x_n;\theta)$. At the best fit value, the partial derivative with respect to each of the parameter becomes 0:

$$\frac{\partial \chi^2}{\partial \delta} = 0, \quad \frac{\partial \chi^2}{\partial \phi} = 0, \quad \frac{\partial \chi^2}{\partial c} = 0. \tag{9}$$

These conditions yield a set of linear equations, the matrix formula of which is

$$\begin{pmatrix} F_0 & F_1 & F_2' \\ F_1 & F_2 & F_3' \\ F_2' & F_3' & F_4' \end{pmatrix} \begin{pmatrix} \delta \\ \phi \\ -\frac{1}{2}c \end{pmatrix} = \begin{pmatrix} Y_0 \\ Y_1 \\ Y_2' \end{pmatrix}, \tag{10}$$

where F_j, F_j', Y_j, and Y_j' are defined as

$$F_j \equiv \sum \frac{1}{\sigma_n^2}(x_n)^j, \quad F_2' \equiv \sum \frac{1}{\sigma_n^2} I_n, \quad F_3' \equiv \sum \frac{1}{\sigma_n^2} x_n I_n, \quad F_4' \equiv \sum \frac{1}{\sigma_n^2} I_n^2, \tag{11}$$

$$Y_j \equiv \sum \frac{1}{\sigma_n^2}(x_n)^j y_n, \quad Y_2' \equiv \sum \frac{1}{\sigma_n^2} I_n y_n. \tag{12}$$

The solution of the curvature, $-c/2$, is then

$$-\frac{1}{2}c = \frac{1}{|\mathbf{A}|} \begin{vmatrix} F_0 & F_1 & Y_0 \\ F_1 & F_2 & Y_1 \\ F_2' & F_3' & Y_2' \end{vmatrix} = \sum y_n Q_n' / |\mathbf{A}|, \tag{13}$$

where $\mathbf{A}$ and Q_n' are defined as

$$\mathbf{A} \equiv \begin{pmatrix} F_0 & F_1 & F_2' \\ F_1 & F_2 & F_3' \\ F_2' & F_3' & F_4' \end{pmatrix}, \tag{14}$$

$$Q_n' \equiv \frac{1}{\sigma_n^2}\{(F_1F_3' - F_2F_2') + (F_1F_2' - F_0F_3')x_n + (F_0F_2 - F_1^2)I_n\}. \tag{15}$$

The standard deviation of the curvature is

$$\begin{aligned} \sigma_c^2 &= < c^2 > - < c >^2 \\ &= 4\sum_{n,m}\{< y_n y_m > - < y_n >< y_m >\} Q_n' Q_m' / (|\mathbf{A}|)^2. \end{aligned} \tag{16}$$

Since the measurements at x_n and x_m are independent,

$$< y_n y_m > - < y_n >< y_m >= \sigma_n^2 \delta_{nm}. \tag{17}$$

Therefore,

$$\sigma_c^2 = 4\sum_n \sigma_n^2 Q_n'^2 / (|\mathbf{A}|)^2. \tag{18}$$

Recalling the equation (5), we get

$$\sigma(\frac{1}{p_t}) = \frac{2}{qB_0} \frac{\sqrt{\sum \sigma_n^2 Q_n'^2}}{|det(\mathbf{A})|} \tag{19}$$

The rms error of $1/p_t$ is therefore given as the function of F_j and F_j'.

2.3 Parametrization of a nonuniform magnetic field

It is not essential to parametrize the nonuniform magnetic field in the evaluation of the momentum resolution. We can numerically calculate $I(x;\theta)$. However, if the magnetic field is parametrized with a set of polynomial functions, we can get analytic form for the momentum resolution and the calculation becomes much easier. Utilizing the cylindrical symmetry, we parametrize the nonuniform field with 4th-order polynomial functions:

$$\begin{aligned} B_z(r,z) &= B_0[1+\alpha(r^2-2z^2)+\beta(r^4+\frac{8}{3}z^4-8r^2z^2)], \\ B_r(r,z) &= B_0[2\alpha rz+\beta(4r^3z-\frac{16}{3}rz^3)]. \end{aligned} \tag{20}$$

The magnetic field lines of the Type-S in EOI are plotted in Fig.1. The cylindrical coil and the flux return yoke are also shown. The inner radius of the coil is $r = 195$ cm, and the outer radius is 205 cm. Its half length is 430 cm. The corner corresponds to $\eta = 1.5$. For this magnetic field, we get

$$\begin{aligned} B_0 &= 2 \ \text{tesla}, \\ \alpha &= 6.961\times10^{-3} \ \text{m}^{-2}, \\ \beta &= -3.287\times10^{-4} \ \text{m}^{-4}. \end{aligned} \tag{21}$$

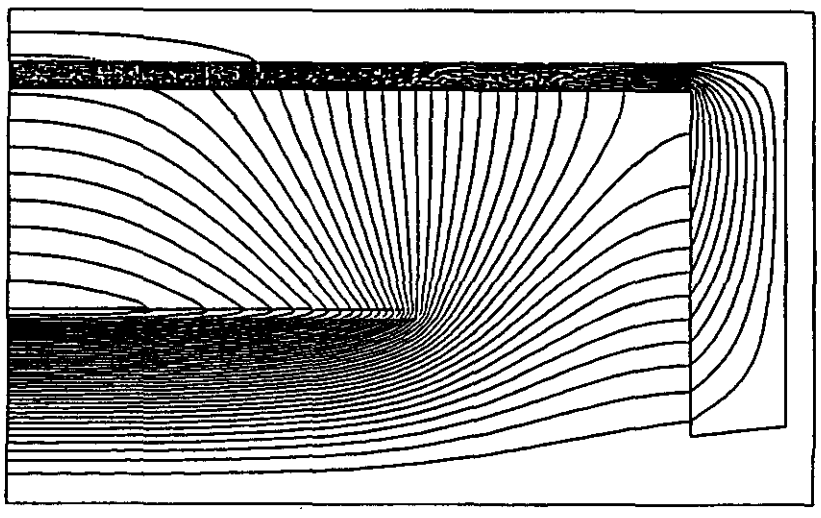

Fig.1. Magnetic field lines of the Type-S coil.

Goodness of the parametrization is shown in Fig.2 for η = 0, 0.5, 1.0, 1.5, 2.0 and 2.5. The upper figure shows B_r versus radius ($\eta = 0, 0.5, 1.0, 1.5$) or z-coordinate ($\eta = 2.0, 2.5$), the lower shows B_z, respectively. In each figure, the solid line shows the calculated result with the program code POISSON [4], the dotted line shows the result with the parametrization. The typical difference between the two curves is at most 5%, except at around $z = 4.3$ m, $\eta = 2.0$, where it is about 10%. The parametrization is good enough for the present purpose to compare the momentum resolution in the nonuniform field with that in the uniform field.

For a high-p_t track, we substitute $z = x \cot\theta$ and $r = x$. Equation (3) becomes

$$B(x;\theta) = B_0[1 + \alpha' x^2 + \beta' x^4], \tag{22}$$

where α' and β' are

$$\begin{aligned} \alpha'(\theta) &= \alpha(1 - 4\cot^2\theta), \\ \beta'(\theta) &= \beta(1 - 12\cot^2\theta + 8\cot^4\theta). \end{aligned} \tag{23}$$

Then equation (5) can be given as

$$I(x;\theta) = x^2(1 + \frac{1}{6}\alpha' x^2 + \frac{1}{15}\beta' x^4). \tag{24}$$

Therefore, F_i' can be expressed with F_j,

$$F_2' = F_2 + \frac{1}{6}\alpha' F_4 + \frac{1}{15}\beta' F_6, \quad \text{etc.}$$

Thus the momentum resolution can be expressed as function of F_j,

$$\sigma(\frac{1}{p_t}) = \frac{2}{qB_0} \times (\text{function of } F_j). \tag{25}$$

2.4 Geometry of the tracking devices

As for the tracking devices, we assume a system consists of pixel detectors, silicon detectors, and wire chambers. Its preliminary conceptual design given in EoI of SDC is shown in Fig.3. Since the geometry of the tracking devices in the intermediate region is complicated, we simplified the geometry. Namely, we just extend the wire chambers to $z_{max} = 4.5$ m, and the silicon detectors in the central region to $z_{max} = 3$ m. The wire chamber system consists of 8 superlayers, each of which consists of 8 tube chambers. The diameter is assumed to be 4 mm. The radii, z_{max}, number of layers, and the position resolutions in $r\phi$ are summarized in Table 1.

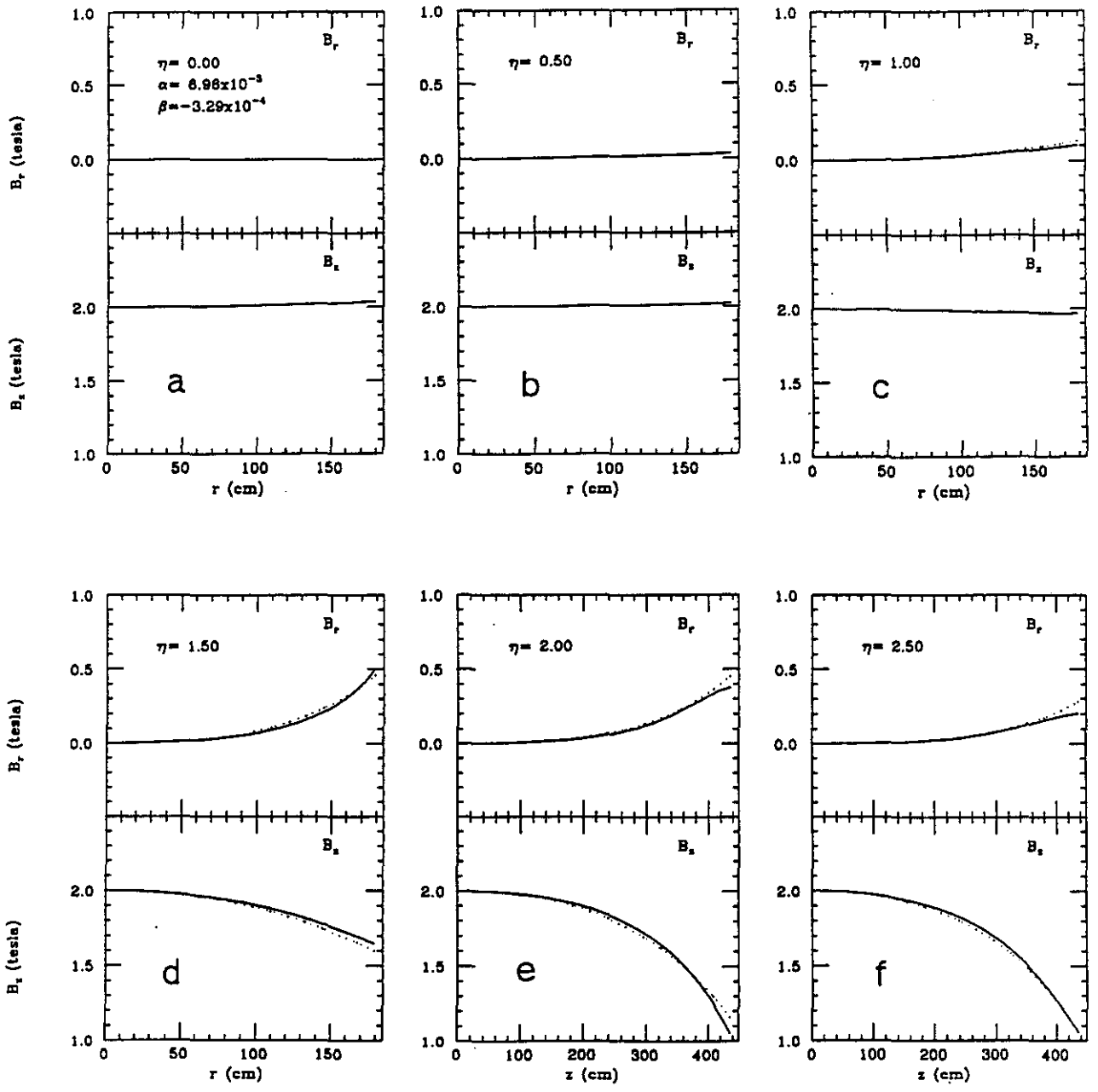

Fig.2. Comparison of the parametrization and the exact calculation of the Type-S field at $\eta = 0$ (a), 0.5 (b), 1.0 (c), 1.5 (d), 2.0 (e), and 2.5 (f). The upper figure shows B_r, the lower shows B_z. Solid curve is the result with the POISSON code, dotted curve shows the parametrization.

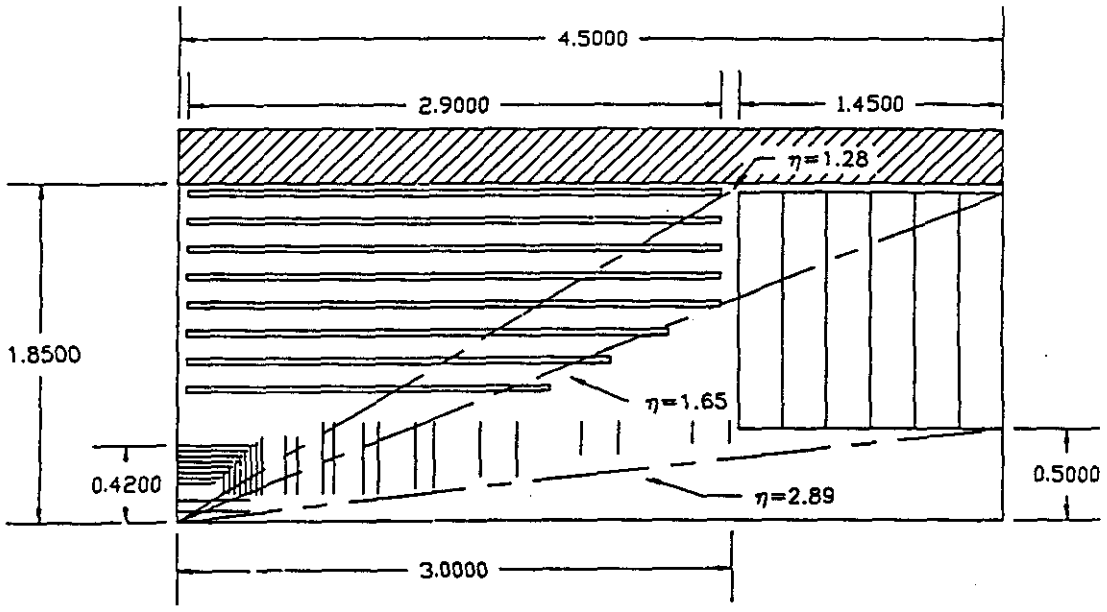

Fig.3. Side view of the preliminary conceptual design of the tracking system given in EOI of SDC. It consists of pixel vertex detectors, silicon strip detectors, and wire chambers.

Table 1. Parameters of the tracking devices.

Tracking device	r_{in} (m)	r_{out} (m)	z_{max} (m)	No. of layers	$\sigma_{r\phi}$ (μm)
Pixel	0.05	0.10	0.4	2	10
Silicon	0.21	0.42	3.0	8	15
Wire	0.72	1.81	4.5	64	150

For simplicity, all the layers of these tracking devices are assumed to provide the $r\phi$-position with the rms error $\sigma_{r\phi}$. Therefore, the absolute value of the momentum resolution itself should not be taken seriously, but taken to be the superior limit. We also assume that the same resolutions can be achieved even in the nonuniform field. The $\mathbf{E} \times \mathbf{B}$ effect in a tube chamber, for example, should be properly corrected.

3 Results

3.1 Type-S vs. uniform field

The transverse momentum resolution at $p_t = 1$ TeV/c versus pseudorapidity, η, is shown in Fig.4. The momentum resolution shown in this report is the one without the vertex constraint, as long as it is not explicitly stated otherwise. The upper figure shows σ_{p_t}/p_t. The solid line shows the Type-S nonuniform field, and the dotted line shows the uniform field. The step-ups in the region $\eta > 1.5$ correspond to the decrease of the number of the superlayers. The momentum resolution in the Type-S field is constant up to $\eta \simeq 1.3$, which is the same as the uniform field. In this region, $\sigma_{p_t}/p_t \simeq 0.09$. The lower figure shows the ratio of the momentum resolution in the Type-S field to that in the uniform field, $\sigma_{p_t}(\mathrm{Type-S})/\sigma_{p_t}(\mathrm{uniform})$. The ratio is unity up to $\eta \simeq 1.0$, then gradually increases to about 1.2 until $\eta \simeq 1.6$. It is almost constant, $1.2 - 1.3$, in the region of $1.6 < \eta < 2.5$.

If we know the magnetic field in the tracking volume, and if we use a proper fitting function, we can get good momentum resolution even with the Type-S field. Compared with the uniform field, it is just 20 to 30 % worse only in $1.6 < \eta < 2.5$. However, one should note that the result is depends on the geometry of the tracking devices.

We studied the momentum resolutions for four cases as shown in Fig.5: (a) all the three tracking devices are ON (same as Fig.4), (b) the pixel detector is OFF, (c) the silicon detector is OFF, (d) only the wire chamber system is ON. Below $\eta = 1$, $\sigma_{p_t}/p_t = 9\%$ for (a), 16% for (b), 16% for (c), and 57% for (d). The ratio $\sigma_{p_t}(\mathrm{Type-S})/\sigma_{p_t}(\mathrm{uniform})$ is also unity in this region in every case. In the case of (b), the ratio is 1.3 to 1.4 in $1.5 < \eta < 2.5$. It is about 10% larger than that of (a). In the case of (c), it is 1.35 in $1.6 < \eta < 2.0$, and larger than 1.5 in $\eta > 2.1$. In the case of (d), it is larger than 1.5 and rapidly increases in $\eta > 1.5$.

Since the field line becomes close to parallel to the particle trajectory in the outer region of the wire chamber system at around $1.5 < \eta < 2.0$, the nonuniformity of the Type-S is most exaggerated in case (d). In practice, however, if we impose the vertex constraint, the situation becomes much better even in case (d). We will see this in subsection 3.3.

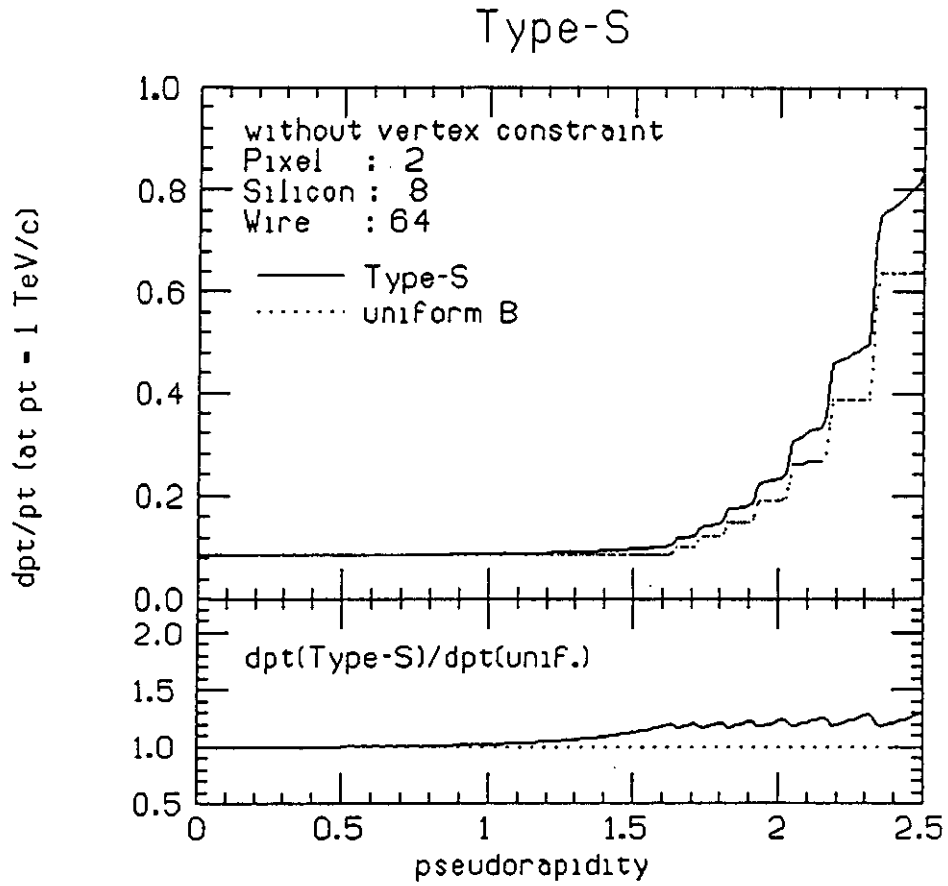

Fig.4. Transverse momentum resolution at $p_t = 1$ TeV/c versus pseudorapidity, η. The upper figure shows σ_{p_t}/p_t, the lower shows the ratio of the momentum resolution in the Type-S field to that in the uniform field, $\sigma_{p_t}(\text{Type}-\text{S})/\sigma_{p_t}(\text{uniform})$. The solid (dotted) line shows the result for the Type-S (uniform) field.

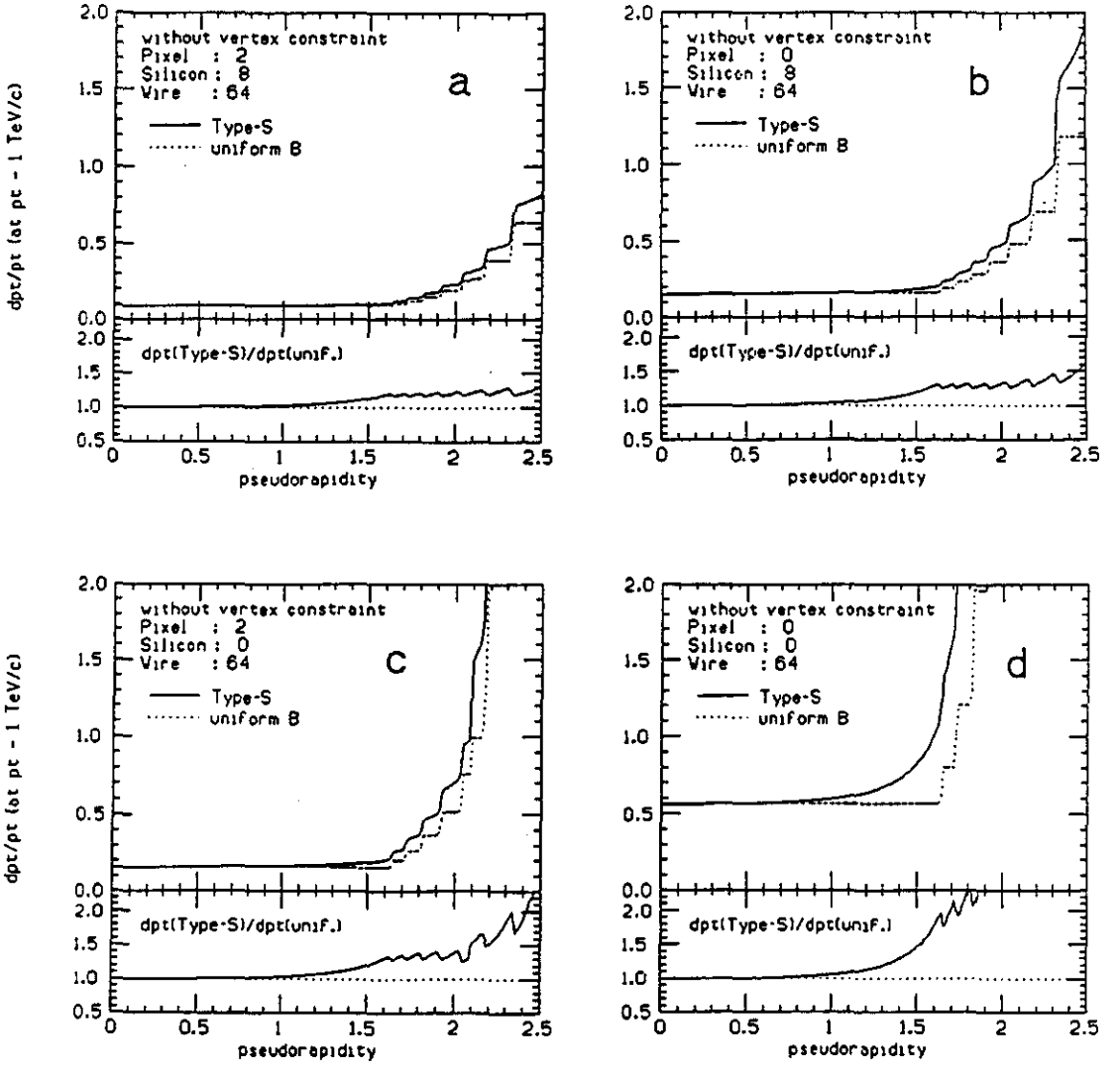

Fig.5. Momentum resolution in the Type-S field when all the three tracking devices are ON (a), the pixel detector is OFF (b), the silicon detector is OFF (c), only the wire chamber system is ON (d).

3.2 Type-G vs. Type-S

We studied effectiveness of a coil with graded current density. Its radius and length are the same as the Type-S coil. The difference is that the current density at the end of the coil is 1.2 times larger for 2 m in length than that in the central region. The field lines of this type, Type-G, are shown in Fig.6. They look alike the lines of Type-S (see Fig.1), but show slightly better uniformity. The field line just outside of the coil shows the typical difference.

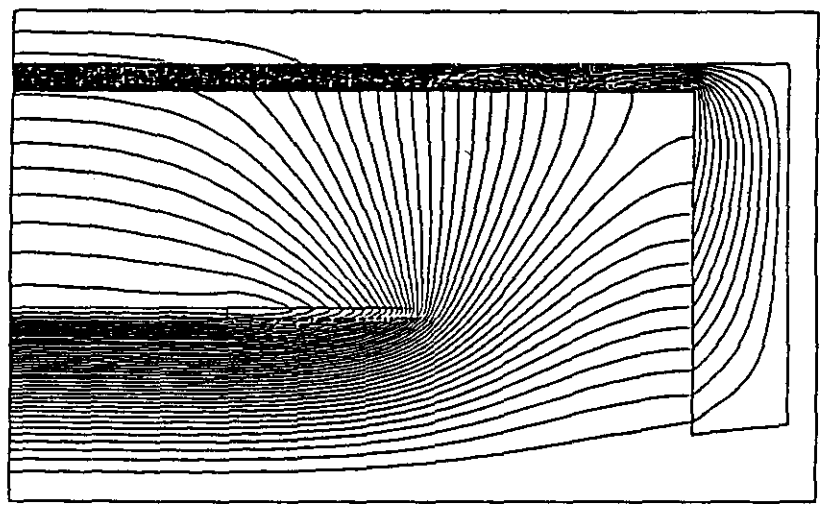

Fig.6. Magnetic field lines of the Type-G coil.

Following the similar analysis as for the Type-S, we estimate the momentum resolution in the Type-G field. Since it is more complicated, the field parametrization of equation (20) is worse in local scale than the Type-S. However, in the global scale, the difference of the parametrized field from the exact field is the same level as the Type-S. The momentum resolution in the Type-G field is compared with that in the Type-S in Fig.7. Interpretation of the figure is the same as Fig.4. The solid line shows Type-G, and the dotted line shows Type-S in this figure, though. The momentum resolution in Type-G is only 5% better than Type-S in $\eta > 1.5$. Being taken account of difficulties in construction of the Type-G coil, merit of choosing such an option seems to be small.

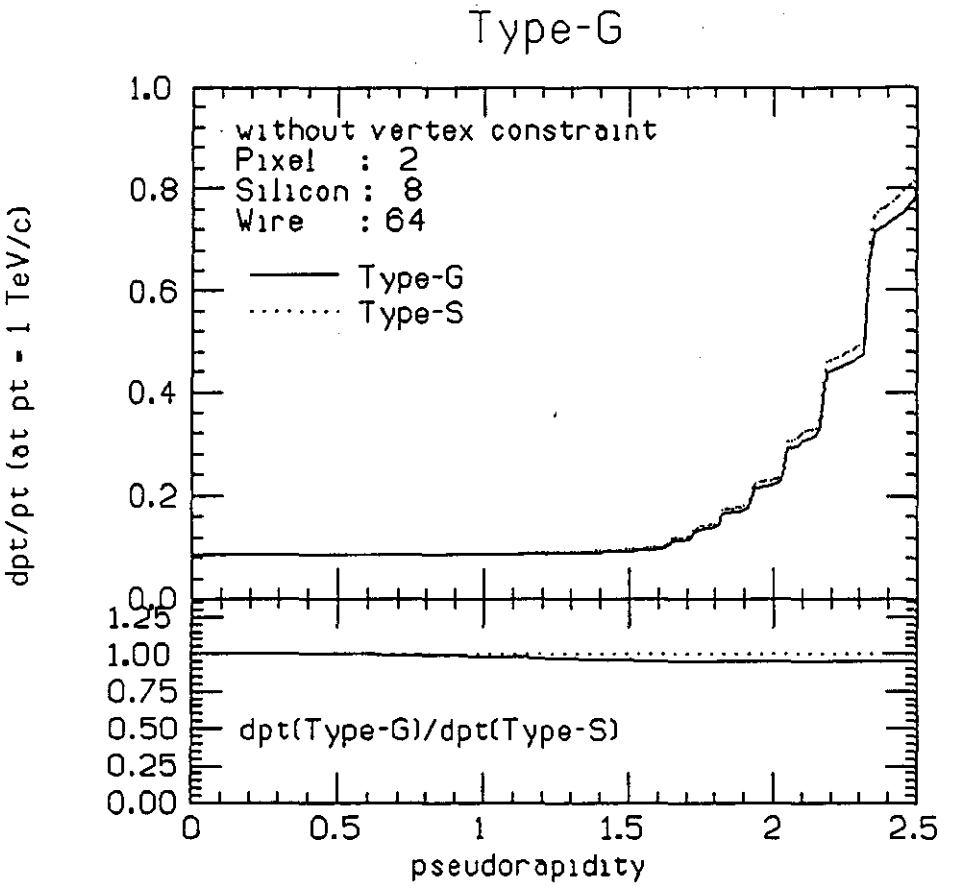

Fig.7. Momentum resolution in the Type-G field, which is compared with Type-S. The solid (dotted) line shows the result from Type-G (Type-S).

3.3 Vertex constraint fit

So far, we have not imposed the vertex constraint on the evaluation of the momentum resolution. We will consider the constraint in this subsection. According to the Conceptual Design of SSC [5], the *rms* beam size is

$$\sigma_x = \sigma_y = 4.8 \ \ \mu\text{m} \tag{26}$$

at the design luminosity, $\mathcal{L} = 10^{33}$ cm^{-2}s^{-1}.

We examined four cases with *rms* vertex constraint, $\sigma_{\text{vtx}} = 5$, 20, 100, and 500 μm. The results are presented in Fig.8: (a) - (c) for $\sigma_{\text{vtx}} = 5\mu$m, (d) - (f) for $\sigma_{\text{vtx}} = 20\mu$m, (g) - (i) for $\sigma_{\text{vtx}} = 100\mu$m, and (j) - ($l$) for $\sigma_{\text{vtx}} = 500\mu$m. The upper figures (Figs.8a,d,g,j) show the results when all the tracking devices are turned ON. The middle figures (Figs.8b,e,h,k) show the results without the pixel detector. The lower figures (Figs.8c,f,i,l) show the results when only the wire chamber system is ON. In all the figures, σ_{p_t}/p_t values are constant up to $\eta \simeq 1.0$. These values versus σ_{vtx} are plotted in Fig.9 together with the results without the vertex constraint.

If all the three tracking devices work, the vertex constraint with $\sigma_{\text{vtx}} > 20\mu$m does not improve the momentum resolution. Without the pixel detector but with the vertex constraint of $\sigma_{\text{vtx}} \simeq 10\mu$m, the momentum resolution is comparable to that with the three devices but without the vertex constraint. Similarly, the wire chamber system alone but with the vertex constraint of $\sigma_{\text{vtx}} \simeq 20\mu$m, corresponds to the case with the silicon devices and the wire chamber system without the vertex constraint (see Fig.8f and Fig.5b). If $\sigma_{\text{vtx}} \simeq 100\mu$m, it is effective only when the wire chamber system alone works. Even if $\sigma_{\text{vtx}} \simeq 500\mu$m, although it does not help in momentum resolution in $\eta < 1.5$, but does help in $\eta > 1.5$ in the last case (see Fig.8l and Fig.5d).

3.4 Tracking volume

We also examined the dependence of the momentum resolution on the tracking volume. The coil radii, its half length, the radii of the wire chamber system, its half length are summarized in Table 2. The geometry of the pixel devices and the silicon detectors is the same as given in Table 1, and it is fixed for all the four cases. The inner radius, the number of superlayers, number of layers in a superlayer, and the position resolution of the wire chamber system are also fixed. The Type-S coil

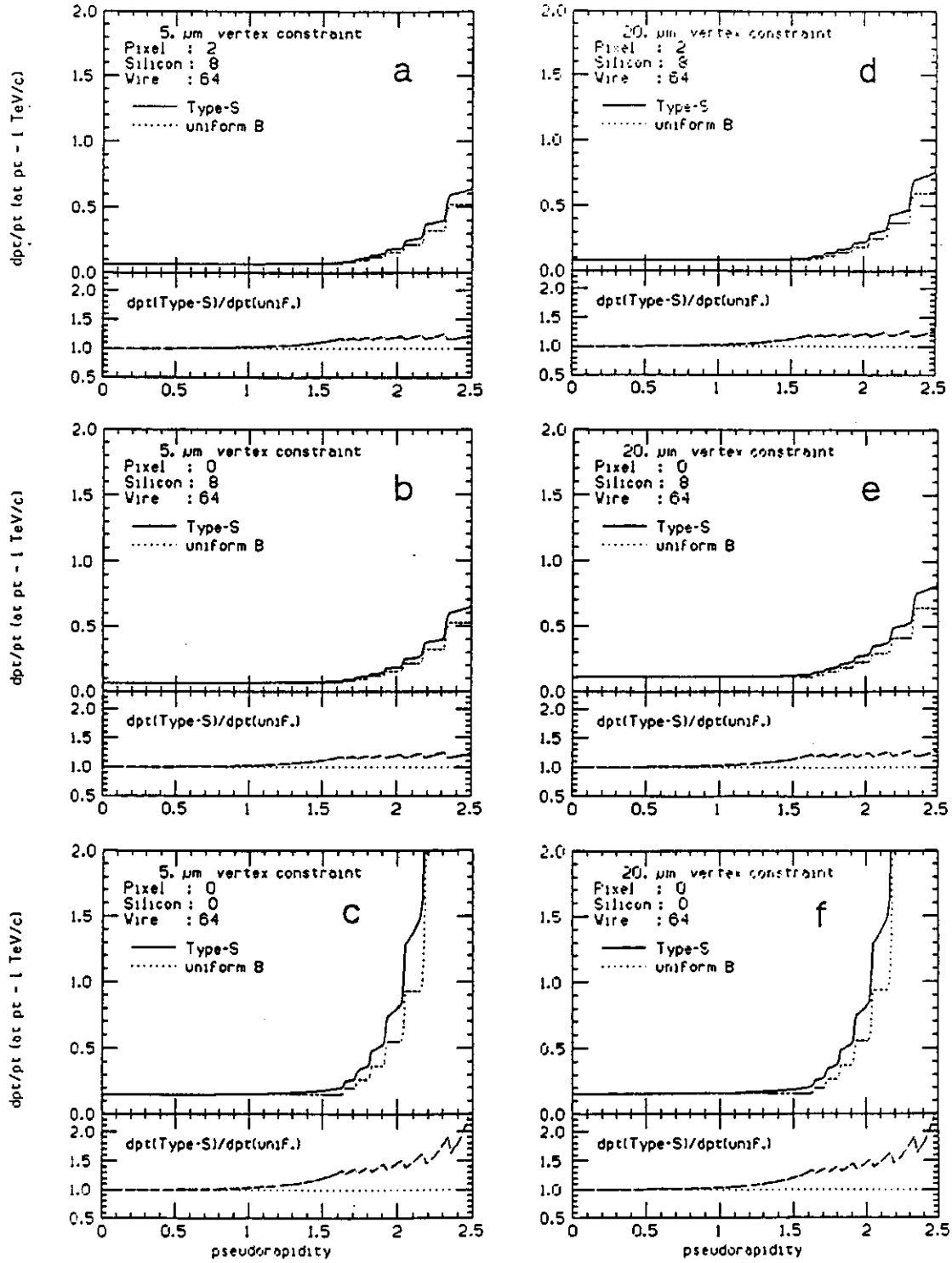

Fig.8. Momentum resolution in the Type-S field with the vertex constraint $\sigma_{vtx} = 5\mu$m (a,b,c), 20 μm (d,e,f), 100 μm (g,h,i), 500 μm (j,k,l). The upper figures (a,d,g,j) show the results when all the three tracking devices are ON, the middle figures (b,e,h,k) are those without the pixel detector, the lower figures (c,f,i,l) are those with the wire chamber system alone.

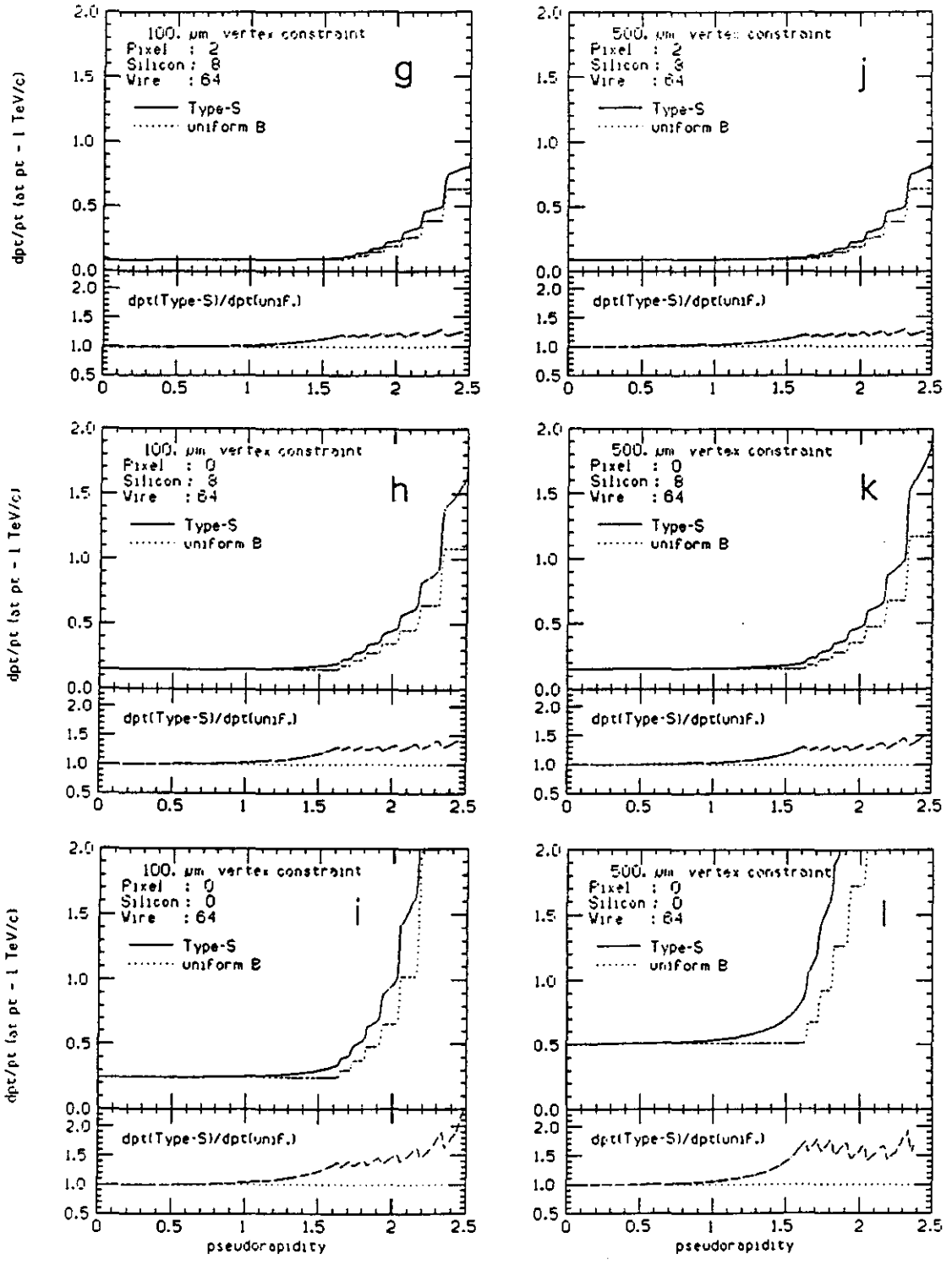
100. μm vertex constraint
Pixel : 2
Silicon : 8
Wire : 64
g
Type-S
uniform B
500. μm vertex constraint
Pixel : 2
Silicon : 8
Wire : 64
j
Type-S
uniform B
100. μm vertex constraint
Pixel : 0
Silicon : 8
Wire : 64
h
Type-S
uniform B
500. μm vertex constraint
Pixel : 0
Silicon : 8
Wire : 64
k
Type-S
uniform B
100. μm vertex constraint
Pixel : 0
Silicon : 0
Wire : 64
i
Type-S
uniform B
500. μm vertex constraint
Pixel : 0
Silicon : 0
Wire : 64
l
Type-S
uniform B
dpt/pt (at pt - 1 TeV/c)
dpt(Type-S)/dpt(unif.)
pseudorapidity

Fig.8.

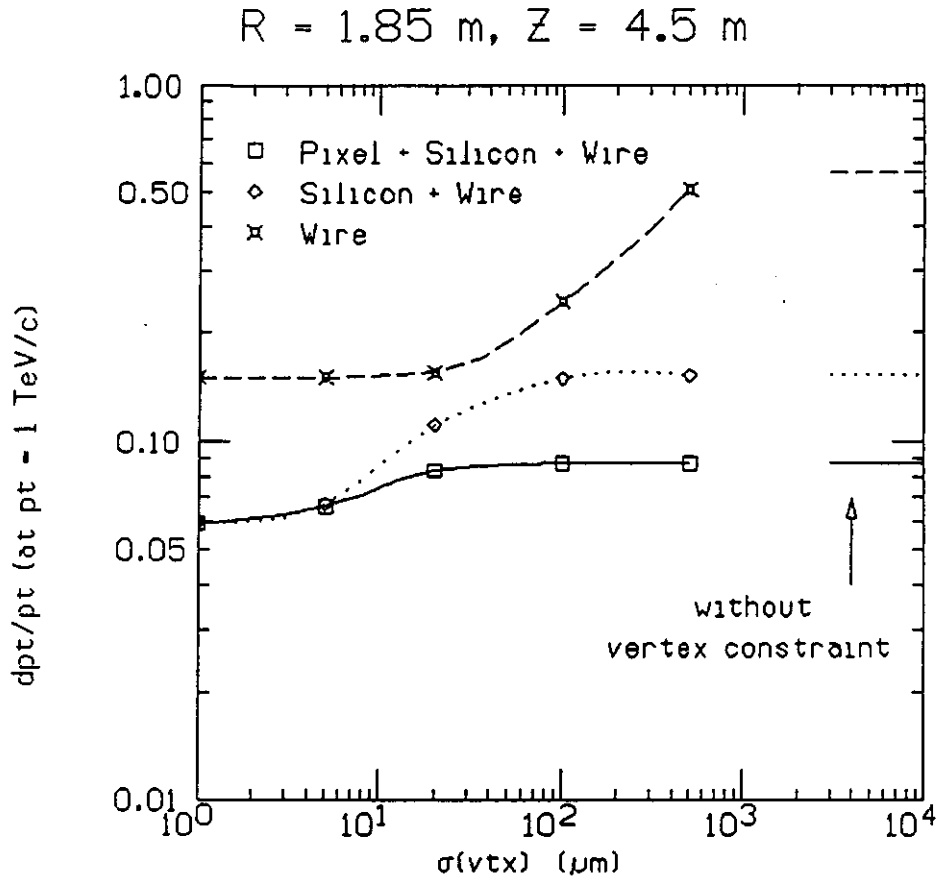

Fig.9. Momentum resolution at $\eta = 0$ versus the *rms* vertex constraint, σ_{vtx}. Results without the vertex constraint are also shown.

is the one which has been considered so far. Type-A is the one with both smaller radius and shorter length. Type-B is the one with the same radius but shorter length. Type-C is the one with larger radius but the same length.

Table 2. Parameters of coil and the wire chamber system.

Type	Coil			Wire chamber			σ_{p_t}/p_t
	r_{in} (m)	r_{out} (m)	z_{max} (m)	r_{in} (m)	r_{out} (m)	z_{max} (m)	at $\eta = 0$ (%)
Type-S	1.95	2.05	4.3	0.72	1.85	4.5	8.7
Type-A	1.65	1.75	3.3	0.72	1.55	3.5	11.5
Type-B	1.95	2.05	3.8	0.72	1.85	4.0	8.7
Type-C	2.25	2.35	4.3	0.72	2.15	4.5	6.8

The resulting momentum resolutions are plotted in Fig.10 (Fig.10a is the same as Fig.4). The values of σ_{p_t}/p_t at the central rapidity region are also given in Table 2. Compared with Type-S, Type-A gives 32% worse momentum resolution (Fig.10b), and its coverage in η is about 0.2 smaller. The coverage of the Type-B becomes $\eta \simeq 0.1$ smaller (Fig.10c). The Type-C gives 22% better resolution with the same η coverage (Fig.10d).

4 Summary

We studied the momentum resolution of high-p_t tracks in a nonuniform magnetic field. In the calculation, we assumed that the tracking devices and their position resolutions were those given in EOI of the SDC group with the simplified geometry. The Type-S field in the EOI proved to give the same resolution up to $|\eta| \simeq 1.0$ and 20 to 30% worse in $1.6 < |\eta| < 2.5$ than the uniform field.

We examined the effectiveness of a coil with graded current density. It provides slightly better uniformity than the Type-S. The momentum resolution is about 5% better in $\eta > 1.5$. However, taken account of difficulties in construction, merit of choosing such an option seems to be small.

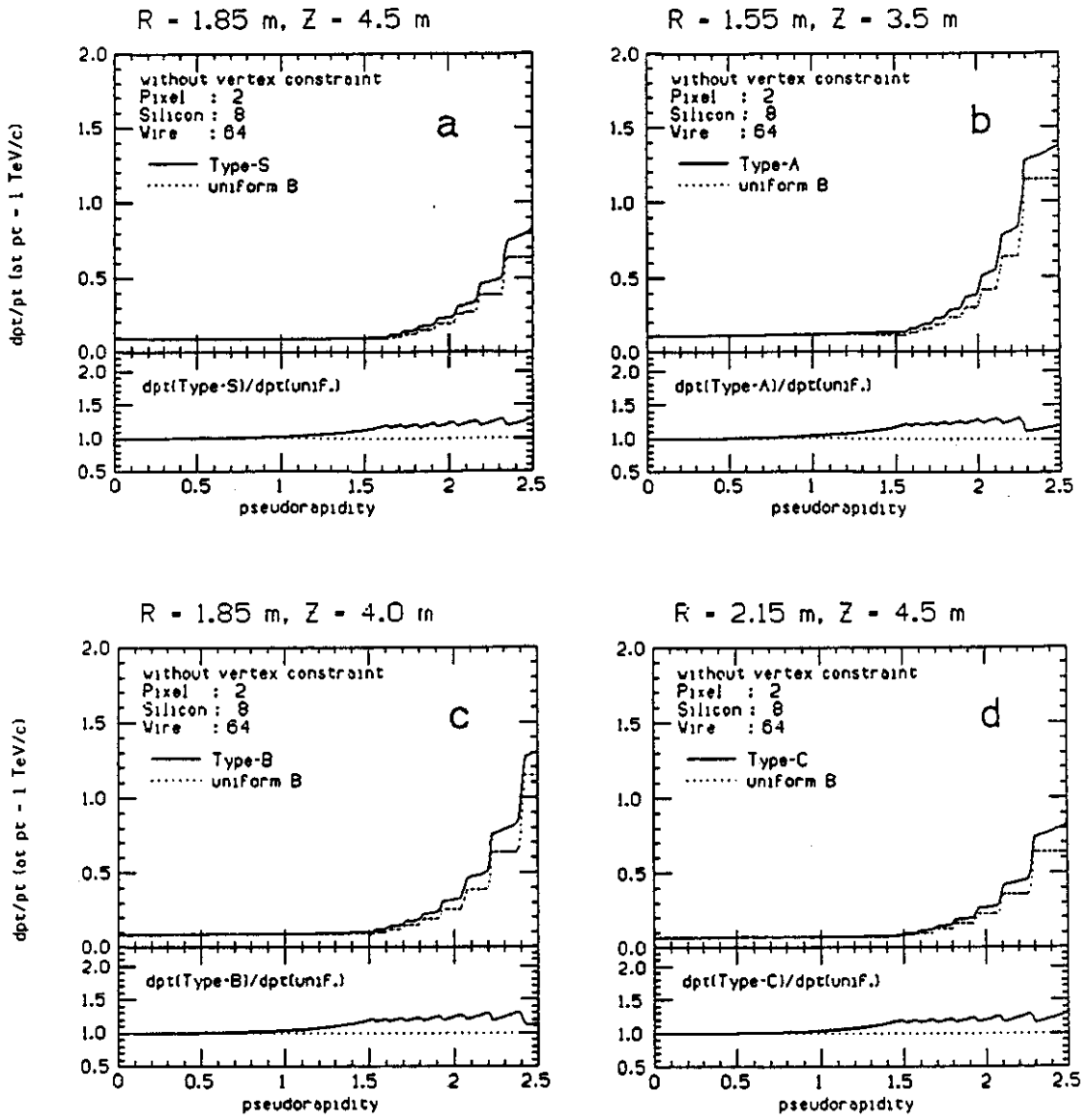

Fig.10. Dependence of the momentum resolution on tracking volume. The types of the coil and the geometry of the wire chamber system are summarized in Table 2. The geometry of the pixel devices and the silicon detectors is fixed. Momentum resolution for Type-S (a), Type-A (b), Type-B (c), and Type-C (d).

If all the three tracking devices work, the vertex constraint with $\sigma_{\rm vtx} > 20\mu$m does not improve the momentum resolution. Without the pixel detector but with the vertex constraint of $\sigma_{\rm vtx} \simeq 10\mu$m, the momentum resolution is comparable to that with the three devices but without the vertex constraint. If $\sigma_{\rm vtx} \geq 100\mu$m, it is effective only when the wire chamber system alone works.

We also examined the dependence of the momentum resolution on the tracking volume. Compared with Type-S, a coil with 15% smaller radius and 23% shorter length gives 32% worse momentum resolution, and its coverage in η is about 0.2 smaller. For a coil with the same radius and 12% shorter length, the coverage becomes $\eta \simeq 0.1$ smaller. A coil with 15% larger radius and the same length gives about 22% better resolution with the same η coverage.

References

[1] A voluntary group, whose members are: F. Abe, K. Amako, H. Iwasaki, T. Kondo, S. Odaka, Y. Sakai, Y. Takaiwa, S. Terada, A. Maki, A. Yamamoto, K. Ueno

[2] Expression of Interest by the Solenoidal Detector Collaboration to construct and operate a detector at the Superconducting Super Collider, 24 May 1990.

[3] R. L. Gluckstern, Nucl. Instr. and Meth. 24 (1963) 381.

[4] M. Cyr and C. Iselin, POISSON, CERN(1976).

[5] SSC Central Design Group, Conceptual Design of the Superconducting Super Collider, SSC-SR-2020, March 1986.